JOURNAL OF GEOPHYSICAL RESEARCH, VOL. 93, NO. A8, PAGES 8532–8544, AUGUST 1, 1988

Nature and the Nonlinear Evolution of Electrostatic Waves Associated with the AMPTE Solar Wind Releases

N. OMIDI

Institute of Geophysics and Planetary Physics, University of California, Los Angeles

K. AKIMOTO

Earth and Space Sciences Division and Applied Theoretical Physics Division, Los Alamos National Laboratory, Los Alamos, New Mexico

D. A. GURNETT AND R. R. ANDERSON

Department of Physics and Astronomy, The University of Iowa, Iowa City

To understand the generation and the nonlinear evolution of the electrostatic waves observed during the AMPTE (Active Magnetosphere Particle Tracer Explorers) solar wind releases, a detailed investigation is conducted. Previous linear studies have indicated that two distinct sets of instabilities may be responsible for the generation of these waves. One set consists of ion acoustic type instabilities which are insensitive to the presence of a background magnetic field, while the other group corresponds to the modified two-stream instabilities and requires the solar wind flow to be across the ambient magnetic field. In order to establish which set of instabilities are more viable for the generation of the observed electrostatic waves a detailed linear Vlasov theory has been conducted by numerically solving the full electromagnetic dispersion relation. In addition, both the plasma wave and the magnetic field measurements by the IRM (Ion Release Module) spacecraft were used to correlate the frequency and the power of the observed waves with the magnitude and the direction of the solar wind magnetic field. The results of these analyses indicate that the ion acoustic type instabilities have growth rates that are an order of magnitude or more larger than those of the modified two-stream instabilities. Similarly, the observations show no correlation between the magnitude and the direction of the ambient magnetic field on the one hand and the wave frequency and amplitude on the other hand, thus indicating that the ion acoustic type instabilities are the likely generation mechanism. In order to investigate the nonlinear evolution of these instabilities and discern their role in the coupling of the released ions to the solar wind, one-dimensional full particle as well as fluid electron electrostatic simulations have been performed. The results show that both the solar wind protons and the released ions can be heated and accelerated in the directions oblique to the solar wind flow velocity.

1. INTRODUCTION

One of the interesting and fundamental problems in the field of space plasma physics is the collisionless interaction between a flowing plasma and newly created ions due to ionization of neutral gases. This type of problem can be present under a variety of physical settings such as during the interaction between the solar wind and comets or interstellar helium gas. Similarly, there have been a number of active experiments in space in which understanding of the interaction between the background plasma and the newly ionized gases has been a primary concern. Among these are the experiments conducted during the AMPTE (Active Magnetospheric Particle Tracer Explorers) mission in which lithium or barium gasses were released in both the solar wind and the magnetosphere. One of the main objectives of these experiments was to trace the motion of the released ions and thereby learn more about the transport properties of the solar wind and the magnetosphere. Clearly, since both the released ions and the background plasma were collisionless, any interaction between the two must have taken place through the electormagnetic forces which were present in the medium prior to the release as well as those that were generated after the release owing to collective plasma processes. Thus in order to gain an understanding of the particle motion, it is necessary to investigate the role of collective plasma processes. In this study the role of wave particle interactions during the AMPTE solar wind releases is investigated.

Paper number 7A9229.
0148-0227/88/007A-9229$05.00

During the AMPTE mission, four releases were made in the solar wind. Of these four, two were lithium releases which took place on September 11 and 20, 1984, and two were barium releases which took place on December 27, 1984, and July 18, 1985. During all of these releases, intense bursts of electrostatic noise were observed on the upstream side of the ion cloud outside of the diamagnetic cavity [*Gurnett et al.*, 1985; *Häusler et al.*, 1986; *Gurnett et al.*, 1986*a*, *b*]. These waves ranged in frequency between tens of Hertz and to several kilohertz, and their peak integrated electric field strength was as high as 40 mV/m. An example of these waves is given in the bottom panel of Figure 1. In this panel the electric field intensities measured by the plasma wave instrument on board the AMPTE/IRM (Ion Release Module) spacecraft during the September 11 lithium release are shown. In this spectrogram the axis of ordinates corresponds to 16 frequency channels ranging from 31.1 Hz to 178 KHz, while the axis of abscissas shows Universal Time (UT). The top three panels in Figure 1 show the magnetic field measurements in geocentric solar ecliptic (GSE) coordinates during the same time period [*Lühr et al.*, 1986]. As can be seen in the third panel, the magnetic field strength falls from its solar wind value ($\sim$6 nT) to nearly zero at 0725:04 UT, indicating the entrance of the IRM space-

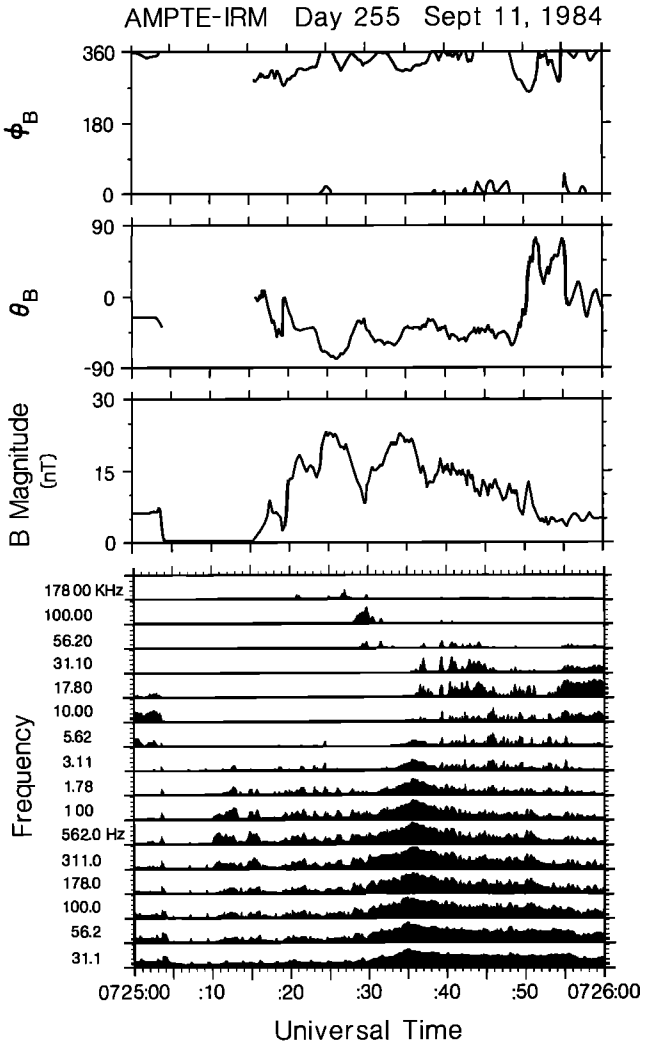

Fig. 1. One-minute measurements by the magnetometer and the plasma wave instrument during the September 11 lithium release in the solar wind are shown. The top three panels show the direction (azimuthal and latitudinal angles in GSE coordinates) and the magnitude of the magnetic field, while the bottom panel shows the electric field spectrogram. The onset of the intense electrostatic waves is at about 0725:30 UT.

craft into the diamagnetic cavity formed by the lithium cloud. As this cloud passes the spacecraft, the magnetic field begins to rise at about 0725:15 UT, reaching values as high as 23 nT. This region of enhanced magnetic field corresponds to a pileup region upstream of the lithium cloud (for a more detailed description of the data, see *Gurnett et al.* [1986*a*] and *Lühr et al.* [1986]). The onset of intense electrostatic waves can be seen in the bottm panel at about 0725:30 UT, reaching peak power at 0725:35 UT. As has been shown by *Gurnett et al.* [1985, 1986*a*] and illustrated in more detail later in this paper, the spectrum of these waves peaks at frequencies between a hundred and a few hundred Hertz.

In order to understand the generation mechanism of the observed electrostatic noise a number of linear studies have been performed [*Gurnett et al.*, 1986*a*, *b*; *Brinca et al.*, 1986; *Papadopoulos et al.*, 1987; *Ma et al.*, 1987]. In the work by *Gurnett et al.* [1986*a*, *b*] it was suggested that the wave amplification takes place via an ion acoustic type instability due to the relative drift between the solar wind and the newly created ions. In these studies, growth rates of the waves with phase velocity along the solar wind flow were calculated and shown to be significant. These studies were later extended to obliquely propagating waves, showing that the growth rates of these waves are comparable to or larger than the parallel propagating waves [*Brinca et al.*, 1986; *Ma et al.*, 1987]. Specifically, it was shown by *Ma et al.* [1987] that two types of instabilities are possible. One is an instability due to the relative drift between the released ions and all the electrons, while the other is due to the streaming between the released ions and the solar wind protons. Both of these instabilities, however, are ion acoustic type in that the wave dispersion properties are similar to those of ion acoustic waves. In fact, using the nonmenclature used by *Gary and Omidi* [1987], the first type of instability corresponds to the electron/ion acoustic, while the second one corresponds to the ion/ion acoustic instabilities. Of primary importance is the fact that these two instabilities are insensitive to the presence of a background magnetic field [*Akimoto and Omidi*, 1986; *Gary and Omidi*, 1987].

In addition to the above set of instabilities, another set has also been suggested by *Papadopoulos et al.* [1987] to be responsible for the generation of the electrostatic waves. These types of instabilities arise when a relative drift between the electrons and ions or two ion species exists across a magnetic field. We will refer to these two instabilities in a collective way as the cross-field instabilities. In these instabilities, it is essential that the electrons be treated as being magnetized, while the ions may be considered unmagnetized. Because the magnetic field in a plasma plays an important role for these modes, the parameter β (the ratio of kinetic to magnetic pressure) can greatly affect the growth rates of these waves. In fact, while these waves are adequately described by the electrostatic dispersion relation at low values of β, electromagnetic effects become important as β increases, until eventually an electromagnetic dispersion relation must be used to discern their properties such as growth rates.

Although, in general, it is possible for all of the above mentioned instabilities to be operative simultaneously, it is much more likely that one of them becomes dominant and thereby governs the nature of the wave-particle interactions during the nonlinear regime. Because our main objective is to discern the role of the observed waves on particle dynamics, it is essential that the likely instability responsible for the generation of these waves be identified. This is the aim of the next section, in which the growth rate calculations of *Papadopoulos et al.* [1987] will be extended by allowing for finite values of β and using the full electromagnetic dispersion relation. In addition, the plasma wave and the magnetic field measurements will be utilized to discern the role of the magnetic field magnitude and direction on the wave properties and thereby deduce the nature of the instability. As will be shown in the next section, the electron/ion acoustic and the ion/ion acoustic instabilities were more likely responsible for the generation of the electrostatic waves.

The nature of the instability having been determined in section 2, a detailed simulation study will be conducted in section 3 to discern the nonlinear evolution of the waves and thereby gain a better understanding of the wave-particle interactions during the AMPTE solar wind releases. The simulations consist of two parts, one in which the electrons and the ions are treated as particles with unrealistic mass ratios. The results of such a simulation study were briefly described by *Omidi et al.* [1987]. The other type of simulation consists of fluid electrons and particle ions. The advantage of this kind of

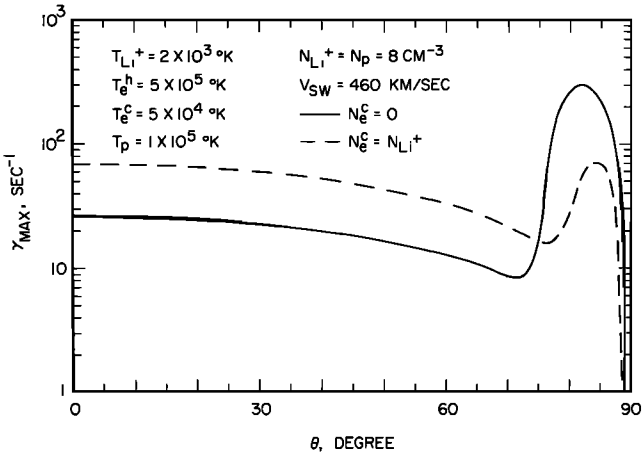

Fig. 2. The growth rates of the ion/ion acoustic and the electron/ion acoustic instabilities maximized over the wave number are shown as a function of the angle (θ) between the **K** vector and the solar wind velocity. The solid line represents the growth rates in the absence of cold electrons, while the broken line corresponds to the case where photoelectrons are present. For the plasma parameters shown, the ion/ion acoustic instability occurs at $\theta \gtrsim 70°$.

simulation method is that realistic mass ratios are used, and thereby the observed plasma parameters can be utilized. A summary and discussion of the results will be presented in section 4.

2. Linear Analysis

2.1. *Theory*

As mentioned earlier, one way in which the viability of the various proposed instabilities in generating the observed electrostatic noise can be tested is by comparing their linear growth rates. To do so, we use a plasma model similar to that given by *Gurnett et al.* [1986*a*] in which the released ions (in this case lithium) form a cold nondrifting Maxwellian with a temperature $T_{Li} = 2 \times 10^3$ °K. The solar wind protons form a Maxwellian with temperature $T_p = 10^5$ °K and a drift speed $V_{sw} = 450$ km/s. As for the electrons, two possibilities were allowed: In one case, the electrons consisted of two separate Maxwellian populations with temperatures $T_e^h = 5 \times 10^5$ °K and $T_e^c = 5 \times 10^4$ °K corresponding to solar wind electrons and those associated with the photoionization of the released gas, respectively; in the other case, only the solar wind electrons were present, allowing for the fact that the colder photoelectrons get replaced by the hotter solar wind electrons. In both cases, the electrons were assumed to have a drift speed such that the net current was zero. It should, however, be mentioned that growth rate calculations with finite current in the plasma were also performed showing no significant difference in the results [see *Gurnett et al.*, 1986*a*]. Finally, in regard to the density ratio of the released ions to the solar wind protons, a wide range of values were considered because the observations show that the density ratio changes considerably with distance from the outer edge of the diamagnetic cavity. The results of linear theory have shown that the growth rates are maximum when the proton and the lithium (or barium) densities are equal, although the growth rates are appreciable over a wide range of density ratios (i.e., 10^{-2} to 10^2). Throughout this paper, we take the density ratio to be 1, noting that our conclusions are insensitive to the choice of this parameter.

Because the growth rate calculations of the ion acoustic type instabilities have been performed in great detail in previous studies [*Gurnett et al.*, 1986*a*, *b*; *Brinca et al.*, 1986; *Ma et al.*, 1987; *Gary and Omidi*, 1987], here we will only summarize the pertinent results. Figure 2 [from *Ma et al.*, 1987] shows the growth rate (γ_{max}) of electrostatic waves maximized over the wave number (K) as a function of θ (the angle between the **K** vector and the solar wind velocity) for the parameters shown in the figure. The solid line represents the case where no cold photoelectrons are present, while the dashed line corresponds to the case where photoelectrons are present. As can be seen, the growth rates decrease monotonically with increasing θ for $\theta \lesssim 70°$. However, beyond this point and in the range $70° \lesssim \theta \lesssim 82°$ the growth rates rise with θ, indicating a change in the nature of the instability. As was pointed out by *Ma et al.* [1987], the growth rates at $\theta \lesssim 70°$ correspond to a kinetic instability due to the relative drift between the electrons and the lithium ions. This instability is similar to a current-driven ion acoustic instability in that the wave growth is due to Landau resonance with the electrons. Using the terminology introduced by *Gary and Omidi* [1987], we refer to this instability as the electron/ion acoustic instability. The growth rates at $\theta > 70°$, on the other hand, correspond to a fluid type instability (for the temperatures considered here) due to the relative drift between the two ion species. This instability was referred to as the ion/ion acoustic instability by *Gary and Omidi* [1987].

It is evident from Figure 2 that in the absence of photoelectrons the ion/ion acoustic instability has a maximum growth rate which is larger than that of the electron/ion acoustic by an order of magnitude. Thus, in the absence of cold electrons the ion/ion acoustic instability is probably the dominant one. On the other hand, the growth rates of the two instabilities are comparable when both electron species are present. This effect comes about by virtue of the fact that the electron/ion acoustic waves grow owing to Landau resonance with the electrons whose distribution function attains a larger slope in the presence of the cold electrons. Similarly, the ion/ion-acoustic waves suffer a greater Landau damping owing to the increase in the slope of the electron distribution function. As was mentioned earlier, these two instabilities are insensitive to the presence of a background magnetic field, and thus one would not expect to see any correlation between the electrostatic waves observed during the AMPTE release and the magnetic fluctuations in the solar wind.

The other set of instabilities which have been proposed to explain the electrostatic noise are the cross-field instabilities [*Papadopoulos et al.*, 1987]. These instabilities also arise owing to a drift either between the electrons and the ions or between two ion species. However, in either case, the drift must be oblique to the direction of the magnetic field with the growth rates becoming maximum when the drift is perpendicular. To help better visualize the geometry of these instabilities, we show in Figure 3 the coordinate system (ρ, η, ζ) in which the solar wind flow velocity (V_{sw}) is along the ρ axis and the ambient magnetic field (B_0) is in the ζ direction. Also shown in Figure 3 is a typical wave vector **K**, which makes an angle Φ with the ζ axis and whose projection on the (ρ, η) plane makes an angle θ with the ρ axis. An important point to note is that unlike the ion acoustic instabilities, the cross-field instabilities are not axially symmetric with respect to the ρ axis, and thus both angle θ and angle Φ play a role in the growth rates of the waves. Another important property of these instabilities is the fact that while in the low β regime

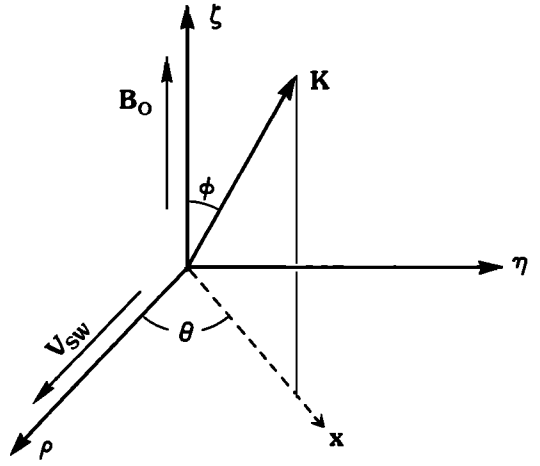

Fig. 3. The relative orientations of the solar wind velocity (V_{sw}), the ambient magnetic field (B_0), and the **K** vector of the waves in the (ρ, η, ζ) coordinate system are shown.

they are well described by the electrostatic approximation, at larger values of β the electromagnetic effects become important and can lead to their stabilization (for more details on the cross-field instabilities, see, e.g., *Gary et al.* [1987]). Since in the analysis of *Papadopoulos et al.* [1987] an approximate dispersion relation was utilized and also the value of β was taken to be zero, it is essential that their study be extended by using a full electromagnetic dispersion relation and allowing for finite values of β.

The general electromagnetic form of the linear Vlasov dispersion equation for a two-dimensional wave vector (**K**) is given by *Tokar and Gary* [1985]. Using this dispersion equation and the plasma parameters described earlier, growth rates have been calculated for a wide range of electron β (β_e) and angles θ and Φ. The results of these computations for the same parameters shown in Figure 2 but without the cold electrons are shown in Figures 4–6. In Figure 4 the growth rates normalized to the proton angular gyrofrequency (Ω_i) and maximized over K are shown as a function of Φ for a number of β_e

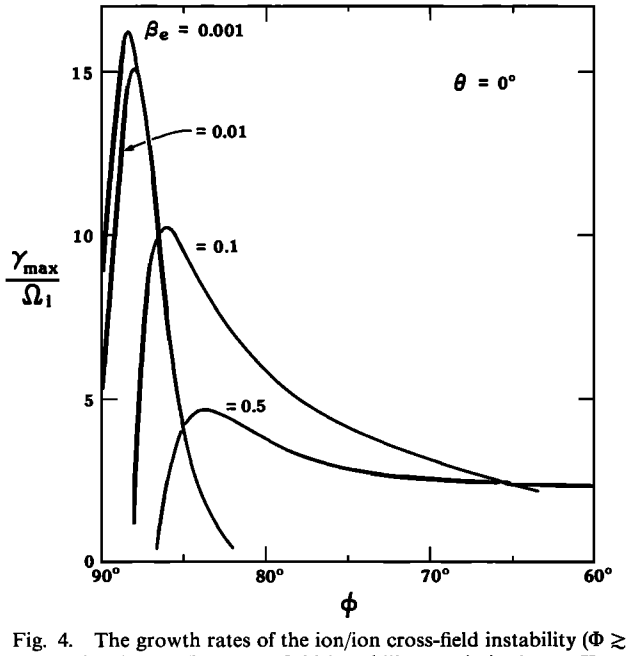

Fig. 4. The growth rates of the ion/ion cross-field instability ($\Phi \gtrsim 88°$) and the electron/ion cross-field instability maximized over **K** are shown as a function of Φ at four values of electron β_e. In this figure $\theta = 0°$, and thus K lies in the (ρ, ζ) plane. Note that as β_e increases, the growth rates become smaller owing to electromagnetic effects. Ω_i is the proton gyrofrequency.

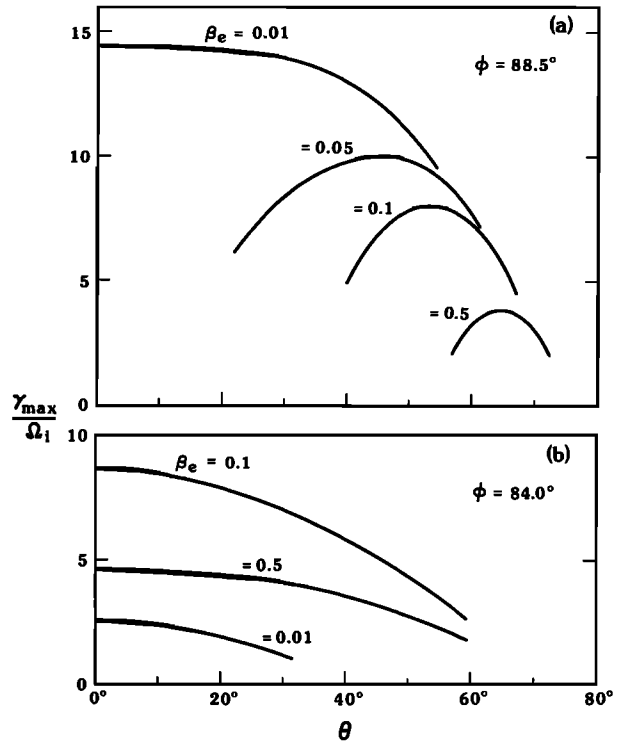

Fig. 5. The growth rates of (*a*) the ion/ion cross-field instability and (*b*) the electron/ion cross-field instability maximized over K are plotted as a function of θ for a number of electron β_e. Note that the growth rates of the ion/ion mode peak at larger values of θ as β_e increases, while the maximum growth of the electron/ion mode occurs at $\theta = 0°$ for all values of β_e.

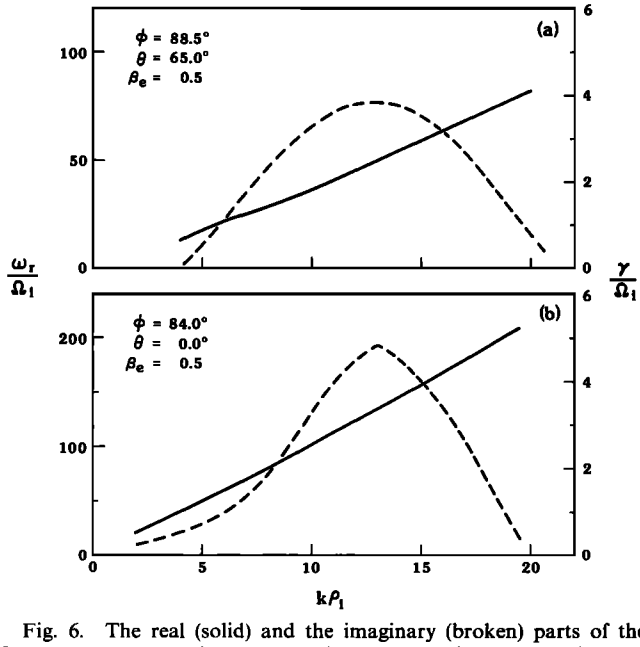

Fig. 6. The real (solid) and the imaginary (broken) parts of the frequency corresponding to (*a*) the ion/ion cross-field and (*b*) the electron/ion cross-field instabilities are plotted as a function of K for $\beta_e = 0.5$ and values of θ and Φ at which maximum growth occurs. The proton gyroradius is represented by ρ_i.

values at $\theta = 0°$. As was mentioned earlier, two types of instabilities are possible when the flow is across the magnetic field. One is due to the relative motion between the electrons and ions and is referred to as the modified two-stream instability, while the other is due to the relative drift between the ions and is referred to as the ion/ion lower hybrid by *Gary et al.* [1987] and the magnetized ion/ion by *Papadopoulos et al.* [1987]. The growth rates shown at $\Phi \lesssim 88°$ are due to the modified two-stream instability, while those at $\Phi \gtrsim 88°$ are due to the ion/ion lower hybrid instability. As can be seen in Figure 4, the latter mode becomes ustable as β_e is increased to about $\beta_e \sim 0.1$. It is also evident that as β_e increases, the maximum growth rates decrease, indicating that the electromagnetic effects become important and tend to stabilize both waves. It should, however, be mentioned that while the ion/ion mode becomes stable at $\theta = 0$ when β_e becomes large, it still remains unstable at other values of θ. To demonstrate this point, we show in Figure 5*a* the maximum growth rates as a function of θ at $\Phi = 88.5°$ for four different values of β_e. The growth rates shown in this panel correspond to the ion/ion lower hybrid instability. As can be seen, when β_e is small (0.01), maximum growth rates peak at $\theta = 0°$. However, as β_e increases, the peak in γ_{max} shifts to higher values of θ. Note that this effect is in contrast to that of the electron/ion mode, whose growth rates are shown in Figure 5*b*. As can be seen in this panel, the growth rates drop monotonically with θ regardless of the value of β_e. Again it is evident in Figure 5*a* that the maximum growth rate of the ion/ion mode decreases with increasing β_e owing to the electromagnetic effects.

A point that should be mentioned in connection with Figure 5*b* is that the growth rates at $\beta_e = 0.1$ are larger than those at $\beta_e = 0.5$ and, in turn, those growth rates are larger than the ones at $\beta_e = 0.01$. This effect is due to the fact that in Figure 5*b*, Φ is kept fixed, while β_e has changed. However, as can be seen in Figure 4, the value of Φ at which γ_{max} peaks varies with β_e. In short, contrary to what might appear in Figure 5*b*, the maximum growth rates of both of the instabilities decrease with increasing β_e.

Thus far the general behavior of the two cross-field instabilities has been investigated for various values of β_e. In order to determine the viability of these instabilities in generating the observed electrostatic noise, it is best to look at the real and the imaginary parts of the frequency as a function of K for a representative value of β_e. Using the plasma parameters given earlier ($n_e = 16$ cm^{-3}, $T_e = 5 \times 10^5$ °K) and a magnetic field strength of 23 nT (see Figure 1), we obtain the value of $\beta_e \sim 0.5$. Note that this value is probably a minimum in that the magnetic field strength used in its computation is the maximum observed value. Using this value of β_e, the real (ω_r) and the imaginary (γ) parts of the frequency have been calculated as a function of K for values of θ and Φ at which maximum growth occurs. Note that the computations were carried out in a frame where the lithium ions are at rest, which should correspond to that of the satellite. Figure 6*a* shows ω_r (solid) and γ (dashed) for the ion/ion cross-field instability, while Figure 6*b* shows those of the modified two-stream instability as a function of the wave number (K) times the proton gyroradius (ρ_i). Using the maximum magnetic field strength observed (23 nT) during the September 11 release, it is straightforward to compute the maximum growth rates of the two instabilities and their corresponding frequency and wavelength. As can be seen in Figure 6, the maximum growth rate of the ion/ion mode is $\gamma \simeq 4\Omega_i \simeq 9$ Hz, while that of the electron/ion mode is $\gamma \simeq 5\Omega_i \simeq 11.3$ Hz. A comparison between these growth rates and those shown in Figure 2 ($\gamma_{max} \sim 300$ Hz) clearly demonstrates that the growth rates of the ion acoustic instabilities are more than an order of magnitude larger than those of the cross-field modes. It is also evident from Figure 6 that the maximum growth of the ion/ion lower hybrid instability occurs at a frequency $f \simeq 17.5$ Hz, while that of the electron/ion occurs at $f \simeq 52$ Hz. Note, however, that these frequencies are too low to explain the observed spectrum. On the other hand, the growth rates of the ion acoustic instabilities become maximum at frequencies of about $f = \simeq 150$ Hz (see, e.g., *Ma et al.* [1987]). Finally, both of the cross-field instabilities have maximum growth at a wave length of about $\lambda \simeq 7$ km, while the wavelength of the ion acoustic waves is of the order of 50–100 m. Given the fact that the radius of the cloud is of the order of 30 km (see, e.g., *Gurnett et al.* [1986*a*]), the wavelengths of the cross-field waves seem to be on the large side, while those of the ion acoustic waves seem more reasonable. Thus the results of linear theory indicate that the ion acoustic instabilities are much more likely to have been responsible for the generation of the observed electrostatic noise.

2.2. *Observations*

In addition to linear theory, the measurements by the plasma wave instrument and the magnetometer can also be utilized to assess the plausibility of each set of instabilities having resulted in the generation of the electrostatic waves. This can be done by noting that while the ion acoustic type instabilities are insensitive to the presence of an ambient magnetic field, the cross-field instabilities result in wave frequencies and growth rates which are sensitive to both the magnitude and the direction of the magnetic field. Specifically, one would expect the wave frequencies of the cross-field instabilities to increase with the ambient magnetic field strength, and also the wave power to rise (fall) as the magnetic field direction becomes more (less) oblique to the solar wind flow direction. Note also that one would not expect the cross-field instabilities to be operative when the solar wind flow is parallel or quasi-parallel to the magnetic field. The September 11 release is particularly suitable for conducting this test in that both the magnitude and the direction of the magnetic field changed considerably during the period when the electrostatic waves were observed [*Lühr et al.*, 1986]. For example, it is evident in the third panel of Figure 1 that the magnetic field varies from $B \simeq 8$ nT at 0725:30 UT to $B \simeq 23$ nT at 0725:35 UT and then drops back to $B \simeq 11$ nT at 0725:38 UT. Similarly, assuming the solar wind flow to be along the Sun-Earth line in the GSE coordinate system (i.e., $\Phi_B = 180°$ and $\theta_B = 0°$), it is clear from the top two panels in Figure 1 that the magnetic field direction changes considerably with respect to the flow velocity.

The eight panels in Figure 7 show the electric field spectrum densities during the period of 0725:30.2–0725:38 UT. The beginning of this period corresponds roughly to the onset of the electrostatic waves, with the power reaching its maximum at about 0725:35. Beyond this time the wave amplitudes decrease, approaching the background level at around 0725:40 UT. One striking feature of the power spectrums shown in Figure 7 is the fact that while the shape of the spectrums changes with time, the maximum power remains at a relatively fixed frequency of $f \sim 150$ Hz. This feature argues against the cross-field instabilities being responsible for the amplification

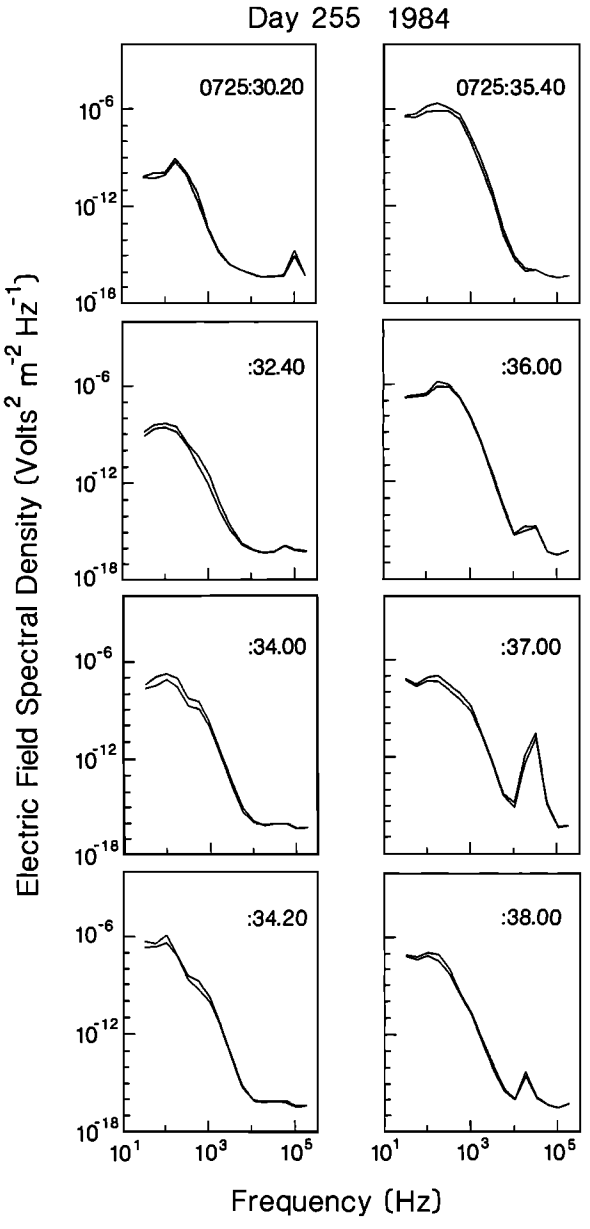

Fig. 7. In this figure, eight electric field power spectrums covering the period 0725:30.2–0725:38 are shown. Note that despite the large changes in the magnetic field strength during this period the frequency at peak power remains relatively fixed ($f \gtrsim 100$ Hz), and at values much larger than those predicted by the cross-field instabilities.

of the waves in two ways. First, the frequencies at peak power are much larger than the frequencies ($f \lesssim 50$ Hz assuming $B = 23$ nT) at which cross-field instabilities have maximum growth rates. Second, since the magnetic field strength varies considerably during the time interval considered in Figure 7, one would expect the frequencies at peak power to vary accordingly. This effect, however, is not reflected in the power spectrums shown in Figure 7. In regard to the direction of the magnetic field it is evident from the top two panels of Figure 1 that both Φ_B (azimuthal angle) and θ_B (latitudinal angle) fluctuate by as much as 30° on relatively short time scales. These fluctuations however, do not seem to affect the intensity of the waves. In addition, while the magnetic field may at times be oblique to the flow direction, it is far from being perpendicular to it, again suggesting that the prevailing conditions in the plasma are not conducive to the generation of waves via the cross-field instabilities.

In short, both theoretical investigations and observational evidence indicate that the electrostatic waves observed during the AMPTE solar wind releases were generated by the ion acoustic type instabilities.

3. Nonlinear Analysis

3.1. *General Remarks*

Thus far we have considered two sets of instabilities with the main distinction between the two being that one set requires the presence of a background magnetic field, while the other can exist in an unmagnetized plasma. Having shown that the ion acoustic type instabilities are the dominant modes, we will devote the remainder of this paper to the nonlinear evolution of the waves. A point to note is that while the electron/ion acoustic and the ion/ion acoustic instabilities result in plasma waves with similar dispersive properties (i.e., acousticlike), it is nonetheless essential that these two instabilities be distinguished when considering their nonlinear evolution. This is because the source of free energy and therefore the saturation mechanism of each instability is different. Specifically, the electron/ion acoustic waves grow owing to Landau resonance with the electrons and therefore, are expected to saturate via quasi-linear diffusion of the electrons and formation of a plateau in their distribution function. Because the time scales associated with this process are small as compared to ion time scales, one would not expect the electron/ion acoustic instability to affect the ions in an appreciable way. On the other hand, the ion/ion acoustic waves grow owing to interaction between the two ion species, and thus their saturation mechanism must involve ions. This can also be seen by noting that any heating of the electrons by the waves will tend to increase the ratio of T_e/T_p, which enhances the growth rates (see, e.g., *Gary and Omidi* [1987]). In other words, electron heating does not have a stabilizing effect on the ion/ion acoustic waves.

As can be seen in Figure 2, when both the cold photoelectrons and the hot solar wind electrons are present, the maximum growth rates of the electron/ion acoustic and the ion/ion acoustic waves are comparable. Thus it is conceivable that both modes may grow, with the electron/ion waves heating the cold electrons and the ion/ion waves interacting mainly with the two ion populations. On the other hand, when no cold electrons are present, the ion/ion mode becomes dominant. Although the effect of waves on the electrons is interesting, our main goal is to see how the newly born ions are affected by the waves, that is to say, how the observed waves could have resulted in coupling between the solar wind protons and the lithium or barium ions. Thus we need only be concerned with the ion/ion mode and investigate its nonlinear evolution. To this end, one-dimensional electrostatic particle simulations have been performed, the results of which are presented here. These results correspond to two classes of simulations; one, in which the electrons and the ions are treated as particles with the disadvantage of an unrealistic mass ratio between the electrons and the ions, and another, using a simulation code, in which the electrons are approximated by a Boltzman fluid. This code has the advantage that the electron to ion mass ratio is realistic and therefore the observed plasma parameters can be used in the simulations.

3.2. *Full Particle Simulations*

The full particle simulation model consists of a one-dimensional periodic box in the direction of the **K** vector (e.g., the x axis in Figure 3 when $\Phi = 90°$). Note that the **K** vector

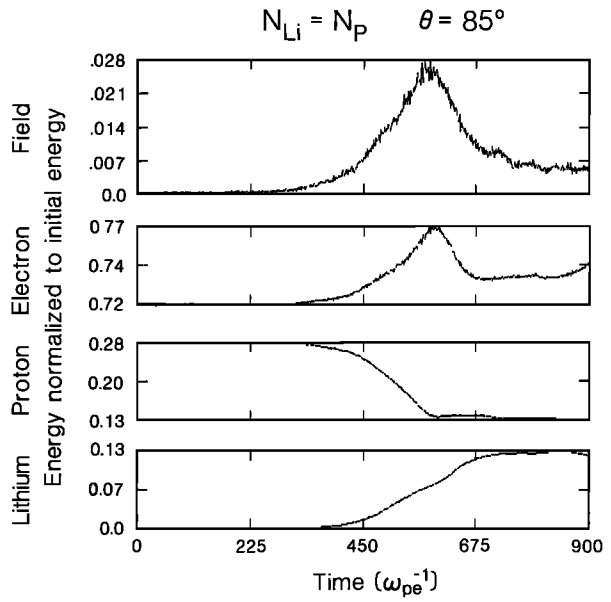

Fig. 8. The energy histories of the electrostatic waves, electrons, protons, and the lithium ions are shown from top to bottom panels, respectively. Note that the energy history of the electrons is similar to that of the waves.

can be directed in any desired direction by assigning the flow velocity of each plasma species to be equal to its original flow velocity projected along the desired direction. Thus, for example, in order to simulate the waves propagating at an angle θ with respect to the solar wind flow direction ($\mathbf{V}_{sw}$) it is sufficient to assign the solar wind velocity to be $V_{sw} \cos \theta$. The simulation results presented in this paper all correspond to a case where no photoelectrons are present, and thus the ion/ion mode has growth rates that are larger than those of the electron/ion mode by an order of magnitude. This is desirable, since our primary interest is in the ion/ion mode. Also, the fact that the ion/ion mode has larger growth rates makes the use of a one-dimensional model appropriate in view of the fact that even in a two-dimensional model the electron/ion modes would not have had a chance to grow. This point will be substantiated later when it is shown that the ions become disrupted on time scales shorter than the growth time of the electron/ion mode. The size of the simulation box is 32 electron Debye lengths (λ_e), and it consists of 64 cells. The simulation frame is taken to be the same as that in the linear theory, and thus initially the lithium ions form a nondrifting Maxwellian, while the solar wind protons consist of a Maxwellian drifting with velocity $V_{sw} \cos \theta$. Similarly, the electrons have a drift speed such that the net current is zero.

As mentioned earlier, one of the difficulties associated with a full particle code is the fact that the simulation must account for the electron dynamics. Therefore the time steps in the simulations must be small enough so that the electron dynamics are resolved. On the other hand, since the ion/ion mode involves the motion of the ions which takes place on a much longer time scale, it is not feasible to use a realistic mass ratio between the electrons and the ions. Thus it is necessary to adjust the ratio of the masses so that both the electron and the ion dynamics can be simultaneously resolved. For this reason, we use $m_{Li} = 6m_p = 600\ m_e$, where Li, p, and e stand for lithium, proton and electron, respectively, and m is the mass.

Although the use of unrealistic mass ratios does not usually change the physical nature of the problem, it does make it impossible to use the exact plasma parameters as those in a realistic plasma. The results of the full particle simulation presented here correspond to the following plasma parameters: the proton flow velocity $V_{sw} = 0.71\ v_e$ and its thermal velocity $v_p = 0.01\ v_e$, where v_e is the electron thermal speed; the lithium thermal velocity $v_{Li} = 0.26 \times 10^{-2}\ v_e$; the angle of propagation $\theta = 85°$; the lithium density $N_{Li} = N_p$. In these simulations the electrons are represented by 32,000 particles, while the protons and the lithium ions are each represented by 16,000 particles. The time step $\Delta t = 0.2\omega_{pe}^{-1}$, where ω_{pe} is the electron plasma frequency. Finally, it should be mentioned that the simulations are carried out as an initial value problem where the system is allowed to evolve in time without a constant refurbishing of new particles.

The four panels in Figure 8 show the energy history of the electrostatic waves, electrons, protons, and lithium ions from top to bottom, respectively. These energies are normalized to the total initial energy in the system. As can be seen in the top panel, initially the wave energy increases with time till it eventually saturates at about $t \simeq 560\ \omega_{pe}^{-1}$. Thus during this period the ion/ion waves are growing with time. Beyond $t = 560\omega_{pe}^{-1}$ the wave energy begins to decrease owing to damping by wave-particle interactions. The damping of the waves lasts until about $t \simeq 700\omega_{pe}^{-1}$, when the level of fluctuations becomes more steady with time. The second panel in Figure 8 shows the energy history of the electrons, which closely mimics that of the waves. This behavior is in contrast to the energy history of the protons and the lithium ions. As can be seen, the protons which are the source of free energy for wave amplification lose energy with time until $t \simeq 560\omega_{pe}^{-1}$. Beyond this point, their energy remains relatively constant with time. The lithium ions gain energy throughout the run, although the rate of increase becomes quite small after $t \simeq 675\omega_{pe}^{-1}$. The behavior of the protons and the lithium ions substantiates the expectation that the ion/ion mode can greatly affect the ions. One of the interesting aspects of Figure 8 is the fact that the energy histories of the electrons and the waves are very similar. This suggests that the observed changes in the energy of the electrons must be for the most part due to coherent motion in the electric field of the waves, rather than random motions which cause an increase in their temperature. This point will be further substantiated later.

To better understand the role of the wave-particle interactions in ion dynamics the phase space density plots (V_x versus x) of the protons and the lithium ions are shown in Figures 9 and 10 at three separate times during the simulations. In these figures the velocity of each species is normalized to its thermal speed. As can be seen in Figure 9*a*, initially the protons form a beam with a drift speed $v_d = 0.71 \cos (85°)\ v_e \simeq 6.2v_p$. At later times when the waves have grown, they begin to interact with the protons (Figure 9*b*), leading to their eventual trapping (Figure 9*c*). Note in Figure 9*b* that six oscillations are present, which agrees with the results of linear theory indicating that modes 5 and 6 are the most unstable ones. From the number of trapping vortices in Figure 9*c*, however, it is clear that mode 5 has become dominant at later times. Note also that the center of the trapping vortices lies around $V_x \simeq 2v_p$, which is reasonable in view of the fact that the phase velocity of the unstable waves is $V_\Phi \simeq 1.7v_p$. The phase space density plots of the lithium ions presented in Figure 10 show that initially, these ions have a zero drift velocity. At later times during the simulation the lithium ions begin to interact with the waves, resulting in the oscillations shown in Figure 10*b*. Note again that six oscillations can be seen during this relatively early stage of the simulation. Figure 10*c* shows the lithium ions becoming trapped, indicating that the nonlinear saturation

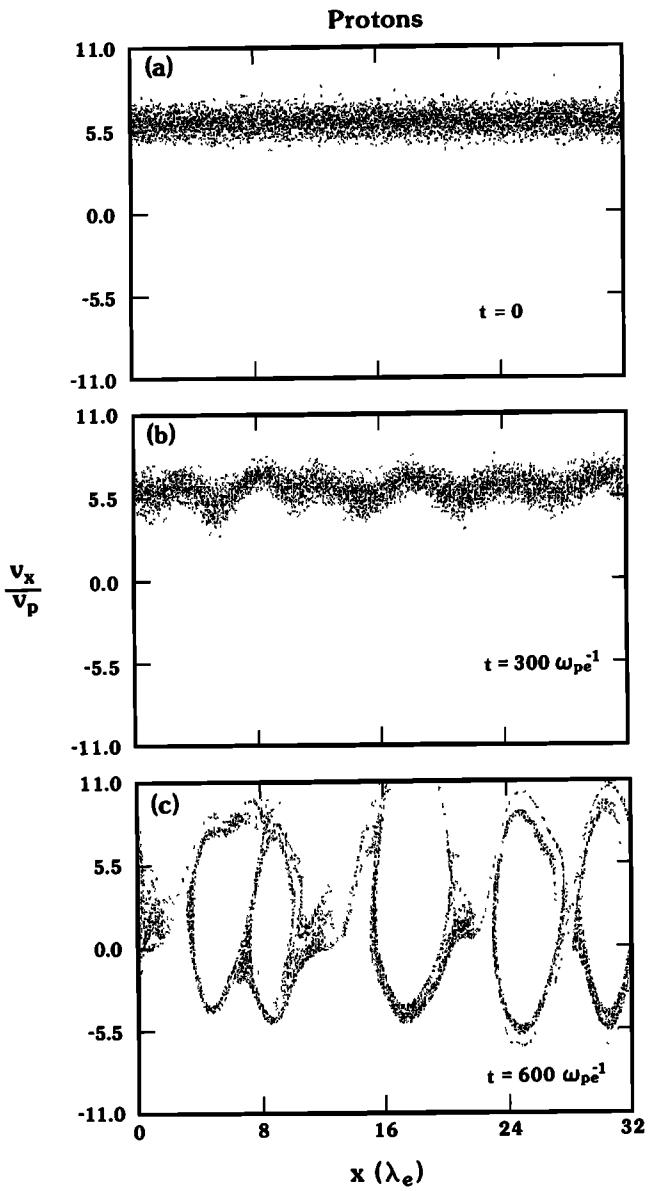

Fig. 9. The phase space density plots of the protons are shown at three different times during the simulations. (*a*) Initially the protons form a beam. At later times they get (*b*) decelerated and (*c*) trapped in the electric potential of the waves, which eventually leads to their scattering in phase space.

mechanism of the ion/ion modes is in this case trapping of both of the ion species. This behavior may at first seem somewhat surprising in that the trapping frequency $\omega_T = (qKE/m)^{1/2}$ (where E is the electric field amplitude and q and m are the charge and mass of the particle) of each species is proportional to the inverse square root of its mass. Thus, ordinarily one would expect the protons to get trapped and saturate the instability before the lithium ions have had a chance to get trapped. The fact that in this case both species suffered trapping can be explained by noting that the phase velocity of the waves, $V_\Phi \simeq 1.7v_p$, falls closer to the lithium ion distribution as compared to that of the protons whose beam speed is $V_d = 6.2v_p$. Thus, in order for the protons to get trapped they must first get decelerated by a substantial amount, and a large electric field must be set up. This, however, requires a longer time, which implies a smaller effective trapping frequency for the protons. In other words, owing to the large flow velocity of the protons relative to the phase speed of the waves, their effective trapping frequency becomes comparable to that of the lithium ions, whose velocity distribution function lies closer to the phase velocity of the waves.

In order to understand in more detail the effect of wave-particle interactions on the electrons, their velocity distribution functions at $t = 0$ and $600\omega_{pe}^{-1}$ are shown in Figures 11*a* and 11*b*. As can be seen, the initial Maxwellian distribution function of the electrons remains unchanged, although the densities (counts) do change with time. Figure 11*c* shows the density profile of the electrons at $t = 600\omega_{pe}^{-1}$. Note that the fluctuations are as much as 50%. The fact that the temperature and the distribution function of the electrons remain unchanged throughout the run further substantiates the suggestion made earlier that the electrons move in a coherent manner in the potential field of the waves. Therefore, as the waves grow, the energy of the electrons also increases, and as waves get damped, their energy decreases. This behavior of the electrons suggests that they may be approximated as a charge-neutralizing fluid when considering the ion/ion mode. Such an

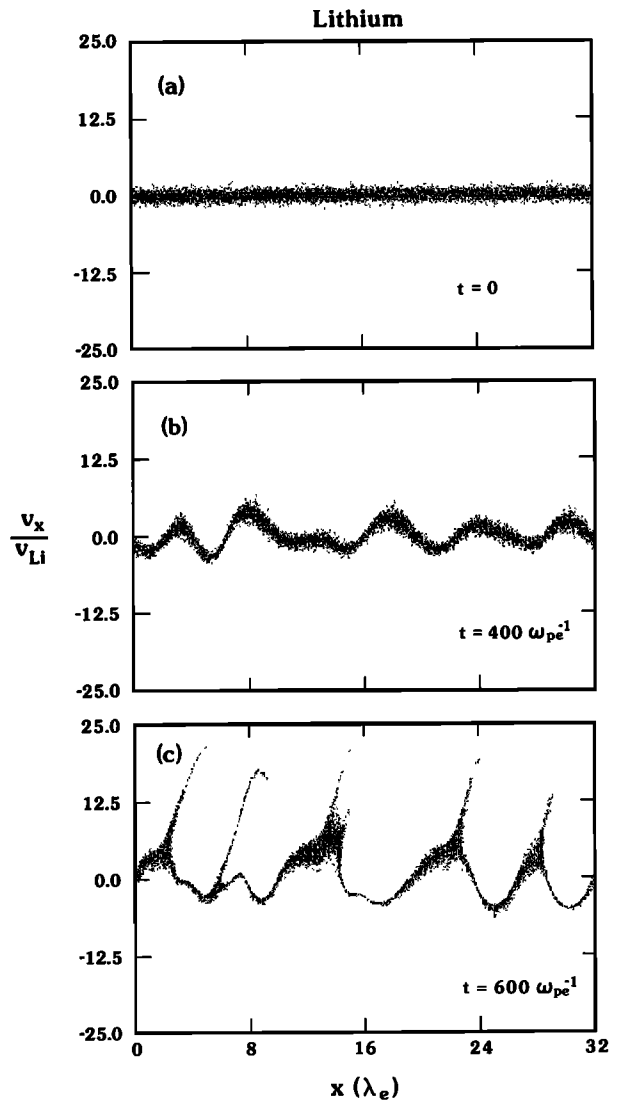

Fig. 10. The phase space density plots of the lithium ions are shown at three different times during the simulations. As can be seen, the lithium ions also interact strongly with the excited waves, leading to their acceleration and eventual scattering in phase space.

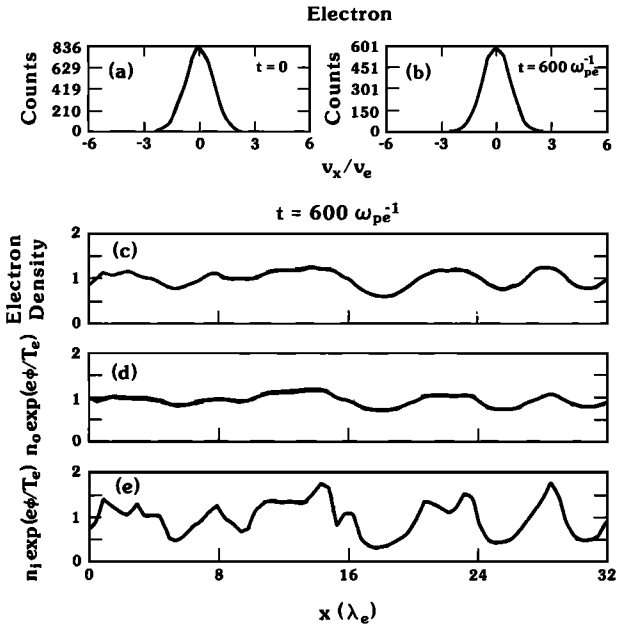

Fig. 11. The velocity distribution functions of the electrons at $t = 0$ and $600\omega_{pe}^{-1}$ are shown. As can be seen, the electrons do not experience any heating due to the wave-particle interactions. Panels show (*c*) the electron density, (*d*) $n_0 \exp(e\Phi/T_e)$, and (*e*) $n_i \exp(e\Phi/T_e)$ as a function of x at $t = 600\omega_{pe}^{-1}$. Note that the electron density profile is best approximated by $n_0 \exp(e\Phi/T_e)$.

approximation is desirable because in the simulations one would not have to be concerned with the electron dynamics, and therefore realistic mass ratios between the electrons and the ions can be used.

3.3. *Simulations With Boltzman Electrons*

To approximate the electrons as a charge neutralizing fluid, use can be made of the Boltzman's relation

$$n_e(x) = n_0 \exp(e\Phi(x)/T_e) \quad (1)$$

which gives the electron density at any position $n_e(x)$ as a function of the electrostatic potential $\Phi(x)$ at that position, the background (or unperturbed) density n_0, and the electron temperature T_e (where the Boltzman constant k is absorbed in T_e). The use of (1) is expected to be quite satisfactory when the density fluctuations are small relative to n_0 and therefore can be thought of as perturbations. On the other hand, once the wave amplitudes become sufficiently large, so that the density fluctuations are a large percentage of n_0, it is not obvious if and why relation (1) should hold. In fact, if the ion density (n_i) fluctuations become large, one might think that a better approximation for the electrons may be to replace n_0 in (1) with $n_i(x)$. To see which one of these methods better approximates the actual density of the electrons, the expressions $n_0 \exp(e\Phi/T_e)$ and $n_i \exp(e\Phi/T_e)$ have been computed at $t = 600\omega_{pe}^{-1}$ and shown in Figures 11*d* and 11*e*, respectively. Note that in our case, $n_i(x)$ is the sum of the proton and lithium densities at position x. A comparison of Figures 11*d* and 11*e* with 11*c* clearly indicates that even in the presence of large amplitude waves, the use of n_0 provides a better approximation to the density of the electrons. Note, however, that even in this case, notable differences between Figures 11*c* and 11*d* exist, suggesting that the Boltzman approximation is not a perfect one.

In order to evaluate the usefulness of the Boltzman approximation in studying the nonlinear evolution of the ion/ion mode, a test simulation run was performed. This run was similar in all aspects (i.e., plasma parameters, mass ratios, etc.) to the full particle run except for the fact that the electrons were approximated by (1). The full nonlinear Poisson's equation was solved for using the Newton iteration method [*Hockney and Eastwood*, 1981]. The phase space density plots of the protons and the lithium ions at $t = 600\omega_{pe}^{-1}$ from the test run are shown in Figures 12*a* and 12*b*, respectively. A comparison between these figures and Figures 9*c* and 10*c* shows that aside from minor details, the results are identical. This clearly demonstrates the validity and the usefulness of the Boltzman approximation in describing the nonlinear physics of the ion/ion instability.

As mentioned earlier, the fluid description of the electrons allows one to use plasma parameters that could correspond to the observation. In the remainder of this section the results of a simulation run with realistic plasma parameters are presented. The length of the simulation box (L) is 64 proton Debye lengths (λ_p) and consists of 64 cells. Each of the ion species is represented by 16,000 particles and the time step $\Delta t = 0.2\omega_{pi}^{-1}$, where ω_{pi} is the proton plasma frequency. Figure 13 shows the growth rates (γ) of the ion/ion instability as a function of the mode number ($LK/2\pi$) for the parameters shown in the figure. These parameters are similar to those used by *Gur-*

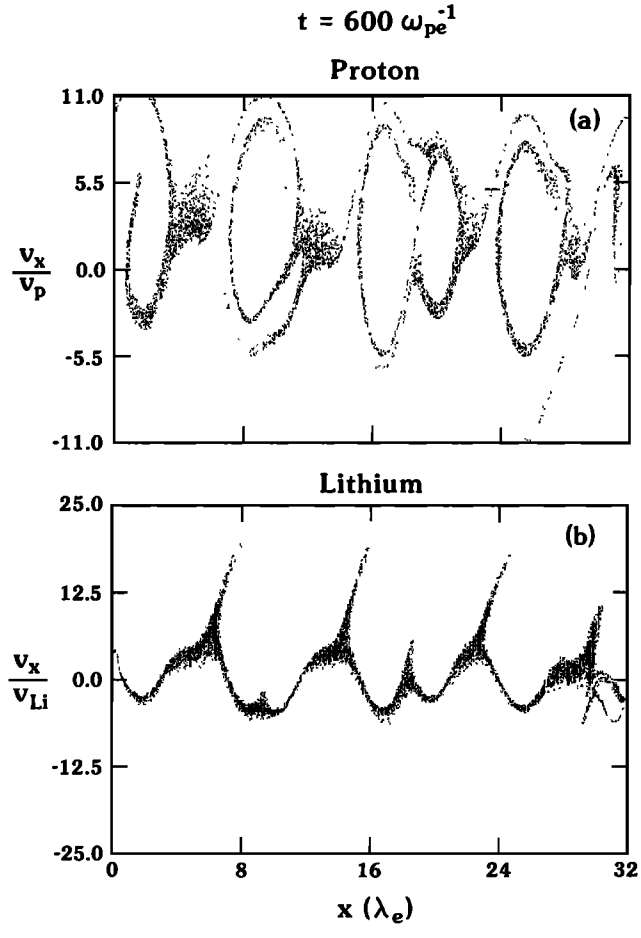

Fig. 12. The phase space density plots of (*a*) the protons and (*b*) the lithium ions obtained from a simulation code with Boltzman electrons are shown. A comparison between Figures 12*a* and 12*b* and Figures 9*c* and 10*c* clearly demonstrates the validity of the Boltzman approximation for the electrons.

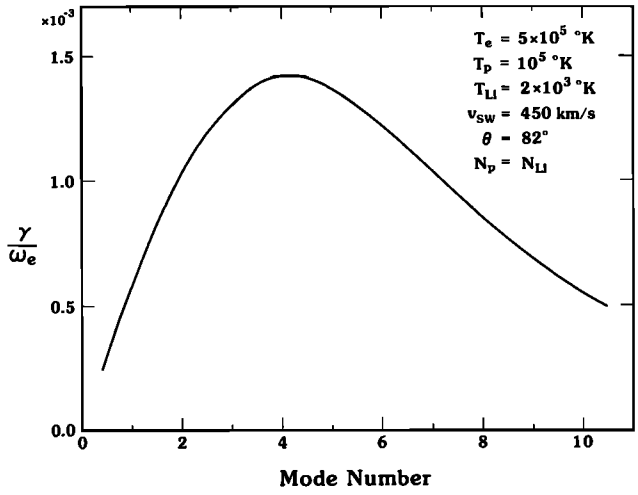

Fig. 13. The growth rates γ of the ion/ion acoustic mode for the plasma parameters shown in the figure are plotted as a function of mode number ($KL/2\pi$). Note that the growth rates peak at mode number 4.

nett et al. [1986*a*, *b*] and are used in the simulation run. As can be seen, the growth rates peak at mode 4, and thus one would expect this mode to be dominant in the simulation. Note, however, that the growth rates of modes 3 and 5 are also appreciable and thus these modes may also show up in the simulations. Figure 14*a* shows the electric field of the waves as a function of x at $t = 60\omega_{pi}^{-1}$ during the simulation. It is evident from this panel that the wave amplitude varies with x or, in other words, is being modulated. To determine which modes have been excited, a Fourier analysis of the electric field squared has been performed and is shown in Figure 14*b*. As can be seen, the peak in the spectrum corresponds to mode 4 with modes 3 and 5 having the second and the third largest power, respectively. This result is in good agreement with the linear theory. Note that although the growth rates of modes 3 and 5 are comparable, one would still expect mode 3 to have larger power because the initial noise level in the system drops with increasing K.

Figure 15 shows the phase space density plot of the protons at three separate times. It is evident in Figure 15*a* that initially the protons have a drift speed $V_d \simeq 2.2v_p$, which is smaller than the beam speed of the protons in the full particle simulation. The phase velocity of the unstable waves $V_\Phi \simeq 0.46v_p$, which falls within the distribution function of the protons. Thus one would expect the trapping of the protons to take place on a faster time scale as compared to the full particle simulation. It can be seen in Figure 15*b* that four trapping vortices have been formed as expected from the Fourier analysis of the waves. Note, however, that the two vortices on the right-hand side of the box are more pronounced because the electric field of the wave is larger on that side of the box. Figure 15*c* shows the protons at a later time when the vortices have begun to collapse, leading to the scattering of the protons in phase space. Note that the vortex on the right-hand side corresponds to the vortex between $32 \lesssim x \lesssim 48\lambda_p$ shown in Figure 15*b*. Similarly, the remnants of the vortex between $48 \lesssim x \lesssim 64\lambda_p$ in Figure 15*b* can be seen at $0 \lesssim x \lesssim 16\lambda_p$ in Figure 15*c*. The observed speed of the vortices is near the phase velocity of the waves, as one would expect.

The phase space density plots of the lithium ions are shown in Figure 16 for the same times as those in the previous figure. Initially, these ions form a cold nondrifting Maxwellian (Figure 16*a*). As the waves grow, the lithium ions are accelerated by their electric field, leading to the observed fluctuations in Figures 16*b* and 16*c*. Note, however, that these ions have not become trapped in the potential well of the waves, in contrast to the protons (see of Figure 15*b*). As mentioned earlier, this behavior is expected, since the trapping time for the lithium ions is longer than that of the protons. The fact that the phase velocity of the growing waves falls within the distribution function of the protons results in their rapid trapping and in saturation of the instability before the lithium ions get trapped. Despite this, however, it is evident that some of

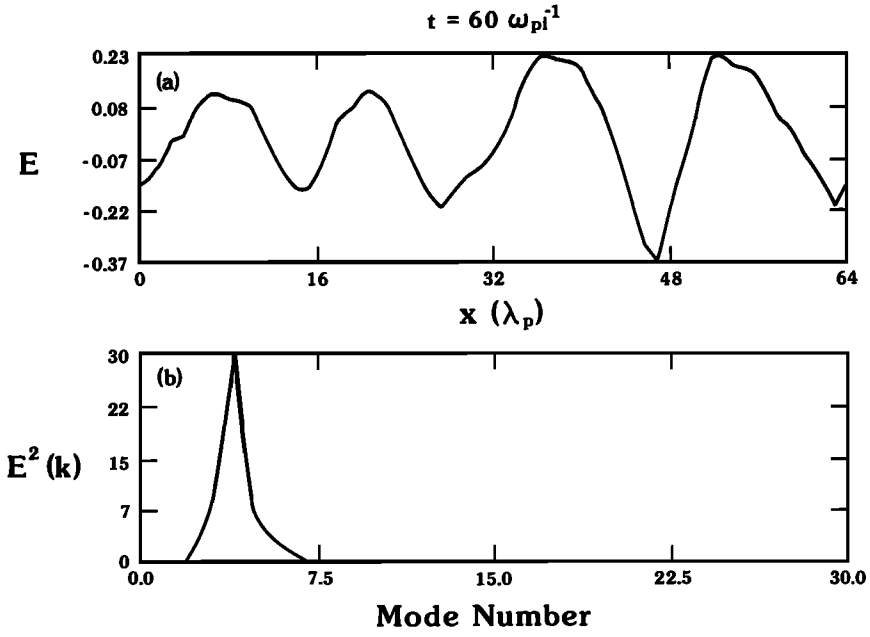

Fig. 14. (*a*) The electric field profile and (*b*) its power spectrum at $t = 60\omega_{pi}^{-1}$ during the simulation are shown. Note that in agreement with linear theory the largest power occurs at mode 4.

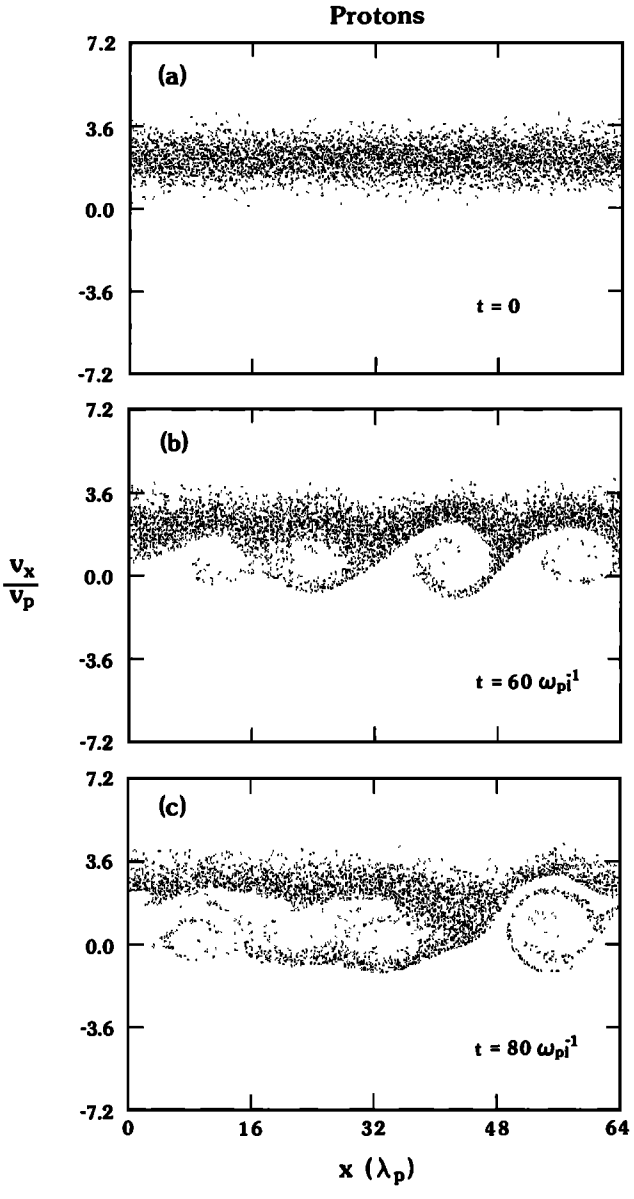

Fig. 15. The phase space density plots of the protons are shown at three different times during the simulations. As can be seen, similarly to those in the full particle case the protons become trapped and later scatter in phase space owing to interaction with the excited waves.

the lithium ions are accelerated to relatively large velocities by the electric field of the waves.

These results clearly indicate that the saturation mechanism of the ion/ion mode remains ion trapping when realistic plasma parameters are used. Nonetheless, differences between the two cases also exist in that the effect of the waves on the heavier ions is not as pronounced when the observed plasma parameters are used. Simulations with barium ions have shown similar results in that the instability saturates via proton trapping and the much heavier barium ions are not strongly scattered in phase space. This is to be expected, since the phase velocity of the waves in the barium case again falls within the proton distribution function, which implies a shorter trapping period for the protons as compared to the barium ions. A point that should also be noted is that the observed heating and acceleration of the ions is along the **K** vector of the ion/ion wave, which is oblique to the solar wind flow velocity. Implications of these results in regard to the role of the ion/ion mode in providing coupling between flowing plasmas and the newborn ions is discussed in the next section.

4. Summary and Discussion

4.1. *Summary*

In this paper the nature and the nonlinear evolution of the electrostatic waves observed during the AMPTE solar wind releases was investigated. By using the full electromagnetic dispersion relation the properties of the modified two-stream and the ion/ion lower hybrid instabilities were studied, and their growth rates were calculated for the plasma parameters representative of those during the AMPTE releases. It was shown that these growth rates are an order of magnitude or more smaller than those of the electron/ion acoustic and the ion/ion acoustic instabilities. Similarly, the frequencies of the

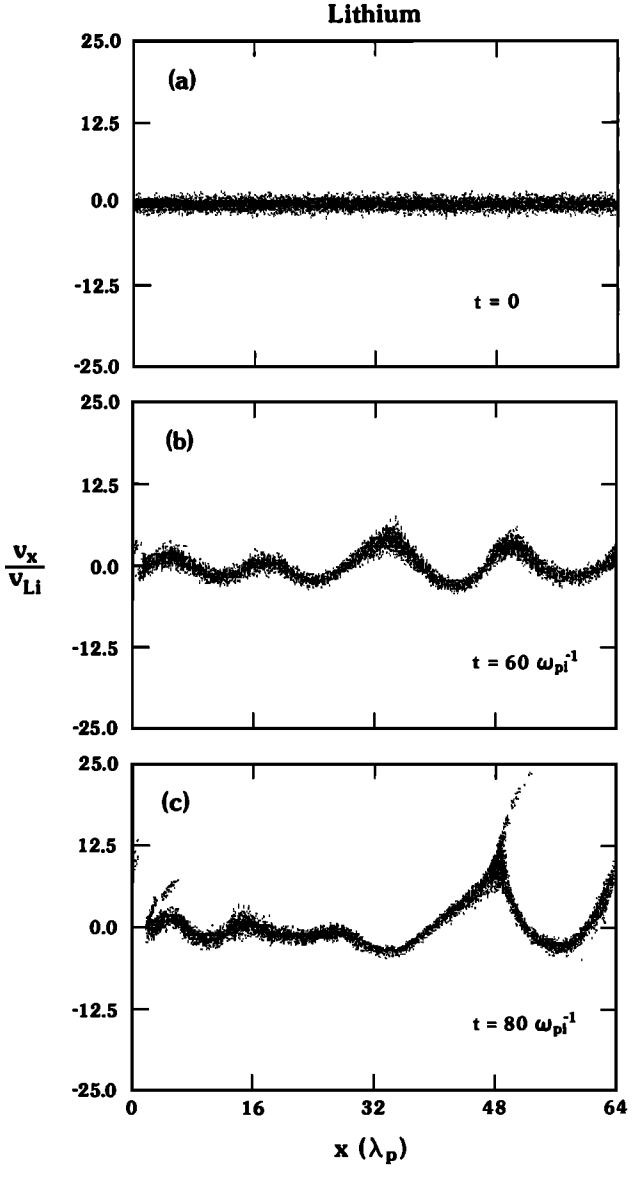

Fig. 16. The phase space density plots of the lithium ions are shown at three different times during the simulations. Note that while these ions undergo some interaction with the waves, they do not become trapped in the potential field of the waves.

cross-field modes were shown to be much smaller than the frequencies at which wave power is observed to peak. This is in contrast to the ion acoustic waves whose maximum growth rates occur at frequencies where the observed noise has maximum power. By using the magnitude and the direction of the ambient magnetic field measured during the September 11, lithium release and also the wave electric field spectrums it was shown that neither the frequency nor the intensity of the observed waves correlates in any clear manner with the changes in the magnetic field. Since one would expect such a correlation to exist had the waves been generated by the cross-field instabilities, it was clear that the observations do not support the suggestion by *Papadopoulos et al.* [1987] that the electrostatic waves were generated by the cross-field instabilities. In view of both theoretical and observational evidence it was concluded that the electrostatic waves associated with the AMPTE solar wind releases were generated by the ion acoustic type instabilities.

Because among the two ion/acoustic type instabilities the ion/ion mode can lead to heating and acceleration of the ions, the nonlinear evolution of this instability was investigated via numerical simulations. By using a full particle electrostatic code it was illustrated that the saturation mechanism of the ion/ion acoustic instability is ion trapping, while the electrons behave as a charge-neutralizing fluid. Because of this characteristic of the ion/ion instability it was possible to conduct a simulation study in which the electrons were treated as a Boltzman fluid, thus allowing for realistic plasma parameters to be used. The results of this simulation study confirmed the conclusions reached by the full particle code that the saturation mechanism of the ion/ion mode is ion trapping and that this process could take place using realistic parameters. In spite of these similarities, however, differences between the two simulation studies also exist. A major difference is that unlike the full particle simulations, in which both the protons and the lithium ions became trapped, in the Boltzman electron simulations, only the protons became trapped. This contrast was attributed to the fact that in the former case the proton drift speed was much larger than the wave phase speed, indicating that the protons would first have to be decelerated and then trapped, thereby increasing their effective trapping period. This increase in the trapping period of the protons then made it possible for both of the ion species to interact strongly with the waves. On the other hand, during the fluid electron simulations the phase velocity of the unstable waves fell within the proton distribution function, resulting in their more rapid trapping. A point to note is that although the calculations presented here correspond to lithium ions, our conclusions are valid for both the barium and lithium releases. This can be seen by the fact that for a given set of plasma parameters the maximum growth rate of the ion/ion acoustic instability scales as $(m_p/m_b)^{1/4}$ [see *Gary and Omidi*, 1987], while that of the ion/ion lower hybrid scales as $(m_p/m_b)^{1/3}$ [*Papadopoulos et al.*, 1987], where m_p/m_b is the ratio of the proton to the released ions mass. Thus, as the mass of the released ions increases, the growth rates of the ion/ion lower hybrid instability drop faster, as compared to those of the ion/ion-acoustic waves. Similarly, the wave spectrum in both types of release has a peak at frequencies close to the ion acoustic frequencies. As for the simulation, from the fact that when realistic plasma parameters are used, lithium ions do not suffer trapping, it is an obvious conclusion that the much heavier barium ions will also not suffer trapping during wave-particle interactions.

4.2. *Discussion*

The results presented here clearly show that the ion/ion acoustic instability can result in transfer of energy and momentum from ions of a flowing plasma to the newly created ions. A question that arises then is how effective this mechanism can be as compared to the other modes that may also be generated owing to the collective plasma processes. Obviously the answer may to some extent depend on the situation under investigation. For example, it was suggested by *Winske et al.* [1984, 1985] that during the AMPTE releases in the solar wind, low-frequency electromagnetic waves could be generated by the ion beam instabilities. However, because of their long wave length in relation to the cloud size these waves could not have been generated in the initial stages of the cloud expansion, and thus the ion/ion acoustic mode would play a dominant role. On the other hand, at times or places (e.g., comets) where the electromagnetic waves can grow to large amplitudes, they become very effective in transferring energy and momentum between the ion species (see, e.g., *Winske et al.* [1984] and *Omidi and Winske* [1987]). Using the plasma parameters of the present simulations, it can be shown that the lithium thermal speed corresponds to $v_L = 1.84$ km/s. From Figure 16*c* it is evident that some lithium ions have been accelerated to velocities as high as 40 km/s, while the majority of the ions have velocities around and below 20 km/s. These speeds, however, are less than 10% of the solar wind flow velocity and therefore not considerable in terms of what is required to assimilate the ions into the solar wind. This is in contrast to the pickup by the electromagnetic waves which can result in average flow velocities for picked-up ions that are 50% of the solar wind speed [e.g., *Omidi and Winske*, 1987]. Nonetheless, the ion/ion acoustic waves may also play an important role in the pickup process. To further investigate this process, it is best to use simulation models with nonperiodic boundary conditions so that a constant refurbishing of the solar wind protons can take place. The advantage of such a model, which is more realistic, is that the instability may not become saturated as early as it does in a periodic system. Similarly, only noninitial value nonperiodic simulations can provide us with an estimate on saturation amplitudes and realistic power spectra which can be compared with the observations. Detection of the electrostatic waves during the AMPTE releases in the solar wind as well as at comet Giacobini-Zinner [*Scarf et al.*, 1986] is good encouragement for conducting such studies in the future.

Acknowledgments. The authors would like to thank H. Lühr for the use of his magnetometer data, and S. P. Gary for the use of his electromagnetic dispersion code. One of the authors (N.O.) would also like to thank K. B. Quest for providing him with the original version of the electrostatic code. The research at UCLA was supported by NASA (STTP) contract NAGW-78, Air Force grant F-19628-85-K-0027, and the National Science Foundation grant ATM85-13215. The work at Los Alamos was supported by the DOE Office of Basic Energy Sciences, Geosciences, and by the Institute of Geophysics and Planetary Physics at Los Alamos National Laboratory. The research at the University of Iowa was supported by the Office of Naval Research through contract N00014-82-K-0183 and by NASA Headquarters through grant NGL-16-001-043.

The Editor thanks R. Pottelette and two other referees for their assistance in evaluating this paper.

REFERENCES

Akimoto, K., and N. Omidi, The generation of broadband electrostatic noise by an ion beam in the magnetotail, *Geophys. Res. Lett.*, *13*, 97, 1986.

Brinca, A. L., A. A. Moreira, F. M. Serra, G. Haerendel, and G.

Paschmann, Complementary analysis and interpretation of the shocklike electrostatic noise observed during the AMPTE solar wind lithium releases, *J. Geophys. Res.*, *91*, 10167, 1986.

Gary, S. P., and N. Omidi, The ion/ion-acoustic instability, *J. Plasma Phys.*, *37*, 45, 1987.

Gary, S. P., R. L. Tokar, and D. Winske, Ion/ion and electron/ion cross-field instabilities near the lower hybrid frequency, *J. Geophys. Res.*, *92*, 10029, 1987.

Gurnett, D. A., R. R. Anderson, B. Häusler, G. Haerendel, O. H. Bauer, R. A. Treumann, H. C. Koons, and R. H. Hozworth, Plasma waves associated with the AMPTE artificial comet, *Geophys. Res. Lett.*, *12*, 851, 1985.

Gurnett, D. A., et al., Analysis and interpretation of the shocklike electrostatic noise observed during the AMPTE solar wind lithium releases, *J. Geophys. Res.*, *91*, 1301, 1986*a*.

Gurnett, D. A., T. Z. Ma, R. R. Anderson, G. Haerendel, G. Paschmann, O. H Bauer, R. A. Treumann, H. C. Koons, R. H. Holzworth, and H. Lühr, Waves and electrical fields associated with the first AMPTE artificial comet, *J. Geophys. Res.*, *91*, 10031, 1986*b*.

Häusler, B., et al., Plasma waves observed by the IRM and UKS spacecraft during the AMPTE solar wind lithium releases: Overview, *J. Geophys. Res.*, *91*, 1283, 1986.

Hockney, R. W., and J. W. Eastwood, *Computer Simulation Using Particles*, McGraw-Hill, New York, 1981.

Lühr, H., D. J. Southwood, N. Klöcker, M. Acuna, B. Häusler, M. W. Dunlop, W. A. C. Mier-Jedrzejowicz, R. P. Rijnbeck, and M. Six, In situ magnetic field measurements during the AMPTE solar wind Li^+ releases, *J. Geophys. Res.*, *91*, 1261, 1986.

Ma, T. Z., D. A. Gurnett, and N. Omidi, An analysis of the shock-like electrostatic noise observed during AMPTE solar wind ion releases, *J. Geophys. Res.*, *92*, 2555, 1987.

Omidi, N., and D. Winske, A kinetic study of solar wind mass loading and cometary bow shock, *J. Geophys. Res.*, *92*, 13409, 1987.

Omidi, N., T. Z. Ma, K. Quest, M. Ashour-Abdalla, D. Gurnett and R. Sydora, Simulation and nonlinear stage of the electrostatic waves observed during the AMPTE lithium release in the solar wind, *Adv. Space Res.*, in press, 1987.

Papadopoulos, K., J. D. Huba, and A. Y. T. Lui, Collisionless coupling in the AMPTE artificial comet, *J. Geophys. Res.*, *92*, 47, 1987.

Scarf, F. J., F. V. Coroniti, C. F. Kennel, D. A. Gurnett, W. H. Ip, and E. J. Smith, Initial report on plasma wave observations at comet Giacobini-Zinner, *Science*, *232*, 1986.

Tokar, R. L., and S. P. Gary, The Whistler mode in a Vlasov plasma, *Phys. Fluids*, *28*, 1063, 1985.

Winske, D., C. S. Wu, Y. Y. Li, and G. C. Zhou, Collective capture of released lithium ions in the solar wind, *J. Geophys. Res.*, *89*, 7327, 1984.

Winske, D., C. S. Wu, Y. Y. Li, Z. Z. Ma, Y. S. Y. Guo, Coupling of newborn ions to the solar wind by electromagnetic instabilities and their interaction with the bow shock, *J. Geophys. Res.*, *90*, 2713, 1985.

K. Akimoto, Earth and Space Sciences Division, Los Alamos National Laboratory, Los Alamos, NM 87545.

R. R. Anderson and D. A. Gurnett, Department of Physics and Astronomy, The University of Iowa, Iowa City, IA 52242.

N. Omidi, Institute of Geophysics and Planetary Physics, University of California, Los Angeles, CA 90024.

(Received July 28, 1987;
revised January 29, 1988;
accepted April 4, 1988.)